Directed evolution of artificial repeat proteins designed as habit modifiers for the morphosynthesis of (111)-terminated gold nanocrystals

*Janak Prasad,[1 #] Sébastien Viollet,[2 #] Kargal L. Gurunatha,[1] Agathe Urvoas,[2] Agathe C. Fournier,[1] Marie Valerio-Lepiniec,[2] Cécile Marcelot,[1] Bulent Baris,[1] Philippe Minard[2] * and Erik Dujardin[1] **

[1] CEMES, CNRS UPR 8011, 29 rue J. Marvig, B.P. 94347, F-31055 Toulouse, France
[2] I2BC, CEA, CNRS, Univ. Paris-Sud, Université Paris-Saclay, 91198, Gif-sur-Yvette cedex, France

[#]: both authors contributed equally to this work

* Corresponding authors: Erik.Dujardin@cemes.fr, Philippe.Minard@i2bc.paris-saclay.fr

Electronic Supplementary Information (ESI)

Table of Contents

A. Materials and Methods

1.Materials. Hydrogen tetrachloroauratetrihydrate ($HAuCl_4$), sodium formaldehyde sulfoxylate (CH_3NaO_3S), hydroxylamine hydrochloride ($NH_2OH.HCl$), monobasic dihydrogen phosphate (KH_2PO_4), dibasic monohydrogen phosphate (K_2HPO_4), calcium chloride dihydrate ($CaCl_2 \times 2H_2O$), phosphate buffer saline (PBS), tris buffered saline (TBS), sodium citrate, hydrochloric acid (HCl), sodium hydroxide (NaOH), dimethylformamide (DMF) and 30% (w/w) hydrogen peroxide were purchased from sigma. Biotin N-hydroxysuccinimide ester (NHS-Biotin), polyethylene glycol sorbitanmonolaurate (Tween 20), Streptavidin, Horseradish Peroxidase, Trypsin (Porcine), 3,3'-Diaminobenzidine (DAB) and 5-nm diameter citrate stabilized Au nanoparticles were purchased from Sigma. Protein LoBind tubes were purchased from Eppendorf. Biotin-PEG-SH (MW: 3000 g/mol) was purchased from Interchim. All reagents were used as received without further purification. Deionized water from a Purelab system (> 18 MΩ.cm) was used in all experiments. pH 7 adjusted 0.01% Tween 20 solution (solution A), PBS solution supplemented with 0.01% Tween 20 (PBST) and TBS solution supplemented with 0.01% Tween 20 (TBST) were prepared*in situ*.

2. Protein expression and purification. αRep proteins were cloned into the plasmid pQE-81 (Qiagen) in order to fuse a His-tag at the N-terminal and were expressed in M15 bacteria strain. Protein productions were performed into 1L of 2YT medium supplemented with kanamycin (50µg/mL) and ampicillin (100µg/mL) from an inoculation of an overnight preculture and grown at 37°C. When an OD600 of 0.6 was reached, bacteria were induced by an addition of IPTG for a final concentration of 0.5mM and were incubated for an additional of 16 hours at 30°C. Cells were harvested by centrifugation, resuspended into 1X TBS supplemented by protease inhibitor (Roche) and frozen until the beginning of the purification procedure. The αRep purification process was carried out by a nickel affinity chromatography (Protino NI-NTA Agarose, Macherey Nagel) followed by a size exclusion chromatography SEC (HiLoad 16/600 superdex 75 pReparation grade column, GE Healthcare) in a phosphate buffer (50mM phosphate buffer pH 7.0, 150mM NaCl). Fractions containing samples of interest were visualized on SDS-PAGE, concentrated and stored at -80°C for further analysis.

A TEV cleavage site was inserted by site directed mutagenesis between the His-tag and the N-terminal extremity of the protein. Purification procedure of modified proteins was performed as previously described and followed by an additional step consisting in the TEV protease cleavage after the SEC: the SEC fractions were collected, mixed with TEV protease (with an OD ratio of 1 TEV protein for 50 proteins of interest) and incubated for 16 hours at 4°C in 50mM phosphate buffer pH 7.0, 150mM NaCl, 1mM DTT and 0.5mM EDTA. A counter purification was made with a nickel affinity chromatography to remove TEV protease from cleaved proteins. Cleavage digestion was checked by SDS-PAGE and fractions containing the αRep were desalted in a phosphate buffer, concentrated and stored.

3. Gel Electrophoresis. To conduct electrophoretic mobility of αRep capped Au seeds, Enduro Gel XL with standard casting set, gel tank with safety lid and power supply, 120 V (E0160) w/FREE UPS was purchased from Labnet International, Inc. A 0.3% agarose gel was prepared by dissolving 300 mg of agarose in 100 mL of 0.5X Tris borate EDTA (TBE) buffer at 90 °C under vigorous stirring. 10 µL of Au seeds were premixed with 2.5 µL of 30% sucrose solution and loaded into sample wells. Electrophoresis was performed at 150 V in 0.5X TBE buffer for 30 min.

S1. Screening and biochemical characterization of αRep

The details of αRep phage display libraries construction and screening has been described in reference [1]. Here, we provided a brief overview of the diversity and screening completeness of this method. Each αRep contains 6 hypervariable positions which implies about 10^5 different repeat units and so 10^{5n} different proteins with n repeat. With an average 3 repeats per protein in our library, this corresponds to a potential of ca. 10^{14} different proteins whereas the library comprises ca. 10^9 clones. A similar ratio is true for the peptides and antibody libraries, which are used in therapeutics.

In practice, in spite of severely limited (10^{-5}) exploration of the entire parameter space, the αRep library, as well as other recent protein libraries such as Darpins,[2,3] have successfully identified binders among the 10^9 clones when selected against numerous biological targets. This implies that there is much more than one effective binder solution for a given interaction scheme. The optimal selection performed in phage display is not the exhaustive exploration of a given parameter space but rather the identification of best suited (within our library) yet probably sub-optimal binders to a given target.

The diversity of our library is indeed practically sufficient to identify a reasonable number of binders for a chosen biomolecular targetand has so far let to the identification of more than 30 biomolecular αRep binders.

Here, we test for the first time the αRep library against an atomically smooth metallic surface. After three runs of phage display selection, about 100 clones where checked for gold affinity by ELISA screening (Fig. S1a). Nine different Au(111) binders are identified, sequenced and characterized (Figs. S1b, c) and their performances as morphosynthetic agents demonstrated in the main text.

The library is thus sufficiently diverse to provide multiple proteins with specific and strong affinity for inorganic surfaces.

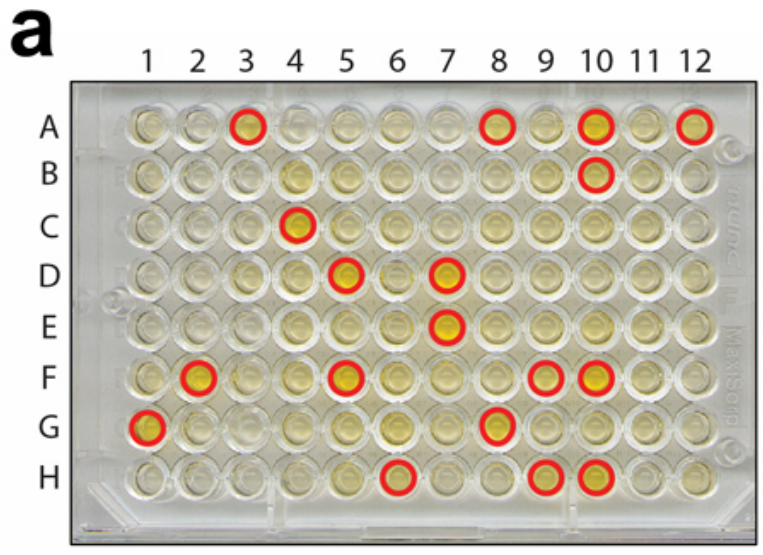

b

α-Rep	N	pI
F2	1	9.00
F5	1	9.05
F10	1	6.05
D7	2	8.89
A12	3	7.97
C4	3	5.67
D5	6	5.42
*bGFPa**	*6*	*5.52*
F9	7	5.30
G8	10	5.19
*N10**	*10*	*5.11*

Figure S1. (a) ELISA screening for high affinity Au(111) binding αRep's. Each well corresponds to one isolated clone obtained after 3 rounds of phage display panning. Bacterial soluble fractions are incubated on the Au(111) film and positive clones (red circles) are revealed using an anti-flagTag HRP antibody (b) Biochemical characterization of Au(111)-selected αRep indicating the number of internal repeats (n) and the estimated isoelectric point (pI).
(*) Proteins marked by an asterisk are used as controls and were not selected against Au(111) but obtained from the consensus sequence (N10) or selected against a Green Fluorescent Protein (bGFPa).[1]

αRep	Repeats	Sequence
A12	N-Cap	TDPEKVEMYIKNLQDDSQRVRNSAANALGKI
	1	GDERAVEPLIKALKDEDWQVRYSAADALGKI
	2	RDERAVEPLIKALKDEDPWVRQSAARALGKI
	3	GDERAVEPLIKALKDEDARVRQAAAYALGKSETNVRLNR
C4	N-Cap	TDPEKVEMYIKNLQDDSTDVRVSAAFALGKI
	1	GDERAVEPLIKALKDEDGYVRLEAALALGKI
	2	GDERAVEPLIKALKDEDDEVRFSAAKALGQI
	3	GDERAVEPLIKALKDEDPFVRIEAARALGQI
	C-cap	GGERVRAAMEKLAETGTGFARKVAVNYLETH
D5	N-Cap	TDPEKVEMYIKNLQDDSRNVRNNAANALGKI
	1	GDERAVEPLIKALKDEDPAVRLSAASALGQI
	2	GDERAVEPLIKALKDEDAYVRLSAAWALGKI
	3	RDERAVEPLIKALKDEDERVRLSAASALGQI
	4	GDERAVEPLIKALKDEDTDVRVAAAEALGEI
	5	GDERAVEPLIKALKDEDGYVRYAAALALGKI
	6	GDERAVEPLIKALKDEDYSVRWAAAAALGQI
	C-Cap	GGERVRAAMEKLAETGTGFARKVAVNYLETH
D7	N-Cap	TDPEKVEMYIKNLQDDSLAVRTFAAIALGKI
	1	GDERAVEPLIKALKDEDKNVRLTAARALGEI
	2	GDERAVEPLIKALKDEDAAVRRTAARALGKI
	C-Cap	GGERVRAAMEKLAETGTGFARKVAVNYLETH
F2	N-Cap	TDPEKVEMYIKNLQDDSTTVRSNAANALGKI
	1	GDERAVEPLIKALKDEDSAVRQSAARALGKI
	C-Cap	GGERVRAAMEKLAETGTGFARKVAVNYLETH
F5	N-Cap	TDPEKVEMYIKNLQDDSNRVRVDAASALGKI
	1	GDERAVEPLIKALKDEDRFVRARAATALGQI
	C-Cap	GGERVRAAMEKLAETGTGFARKVAVNYLETH
F9	N-Cap	TDPEKVEMYIKNLQDDSGEVRVDAASALGKI
	1	GDERAVEPLIKALKDEDATVRQTAASALGKI
	2	GDERAVEPLIKALKDEDSDVRRAAAQALGQI
	3	GDERAVEPLIKALKDEDPTVRLSAARALGQI
	4	GDERAVEPLIKALKDEDSNVRRGAARALGQI
	5	GDERAVEPLIKALKDEDSDVRKTAAQALGEI
	6	GDERAVEPLIKALKDEDGYVRSRAAGALGEI
	7	GDERAVEPLIKALKDEDALVRWAAAEALGKI
	C-Cap	GGERVRAAMEKLAETGTGFARKVAVNYLETH
F10	N-Cap	TDPEKVEMYIKNLQDDSGAVRISAADALGKI
	1	GDERAVEPLIKALKDEDPEVRQAAARALGQI
	C-Cap	GGERVRAAMEKLAETGTGFARKVAVNYLETH
G8	N-Cap	TDPEKVEMYIKNLQDDSGEVRDIAATALGKI
	1	GDERAVEPLIKALKDEDRQVRLAAARALGQI
	2	GDERAVEPLIKALKDEDATVRIAAAKALGEI
	3	GDERAVEPLIKALKDEDRYVRISAALALGKI
	4	GDERAVEPLIKALKDEDVNVRSQAALALGEI
	5	GDERAVEPLIKALKDEDAYVRKEAARALGQI
	6	GDERAVEPLIKALKDEDARVRQSAARALGQI
	7	GDERAVEPLIKALKDEDPDVRIEAADALGEI
	8	GDERAVEPLIKALKDEDTQVRISAAIALGQI
	9	GNERA KALKDEDWQVRKEAARALGQI
	10	GDERAVEPLIKALKDEDGYVRIRAANALGKI
	C-Cap	GGERVRAAMEKLAETGTGFARKVAVNYLETH
bGFPa	N-Cap	TDPEKVEMYIKNLQDDSPPVRVYAAFALGKI
	1	GDERAVEPLIKALKDEDASVRYAAATALGQI
	2	GDERAVEPLIKALKDEDGYVRTAAAEALGQI
	3	GDERAVEPLIKALKDEDPWVRLTAARALGEI
	4	GDERAVEPLIKALKDEDPWVRLTAARALGQI
	5	GDERAVEPLIKALKDEDASVRKAAAVALGQI
	6	GDERAVEPLIKALKDEDEYVRQRAASALGKI
	C-Cap	GGERVRAAMEKLAEPAPGFARKVAVNYLETH
N10	N-Cap	TDPEKVEMYIKNLQDDSWQVRRAAAEALGKI
	1	GDERAVEPLIKALKDEDSDVRRAAAEALGKI
	2	GDERAVEPLIKALKDEDSDVRRAAAEALGKI
	3	GDERAVEPLIKALKDEDSDVRRAAAEALGKI
	4	GDERAVEPLIKALKDEDSDVRRAAAEALGKI
	5	GDERAVEPLIKALKDEDSDVRRAAAEALGKI
	6	GDERAVEPLIKALKDEDSDVRRAAAEALGKI
	7	GDERAVEPLIKALKDEDSDVRRAAAEALGKI
	8	GDERAVEPLIKALKDEDSDVRRAAAEALGKI
	9	GDERAVEPLIKALKDEDSDVRRAAAEALGKI
	10	GDERAVEPLIKALKDEDSDVRRAAAEALGKI
	C-Cap	GGERVRAAMEKLAEPAPGFARKVAVNYLETH

Figure S1c. Sequences of the selected and non-selected αReps. For each protein, each line represent one repeated motif, the first line is the n-Cap, the last line is the C-cap.
Variable residues are highlighted in red.

a

AA	Occurrence	%	Cumul %
Q	29	11.2	11.2
R	27	10.5	21.7
K	27	10.5	32.2
S	27	10.5	42.6
A	24	9.3	51.9
E	19	7.4	59.3
T	15	5.8	65.1
N	13	5.0	70.2
L	13	5.0	75.2
D	12	4.7	79.8
Y	11	4.3	84.1
I	10	3.9	88.0
G	9	3.5	91.5
P	6	2.3	93.8
W	6	2.3	96.1
F	5	1.9	98.1
V	5	1.9	100.0
C	0	0.0	100.0
H	0	0.0	100.0
M	0	0.0	100.0

b

(1)

A12	Ntot	24		
	AA	Occurrence	%	
	Q	4	16.7	16.7
	K	4	16.7	33.3
	R	3	12.5	45.8
	S	3	12.5	58.3

F5	Ntot	12		
	AA	Occurrence	%	
	R	3	25.0	25.0
	S	1	8.3	33.3
	Q	1	8.3	41.7
	K	1	8.3	50.0

F9	Ntot	48		
	AA	Occurrence	%	
	S	7	14.6	14.6
	Q	6	12.5	27.1
	R	5	10.4	37.5
	K	4	8.3	45.8
	T	4	8.3	54.2

F10	Ntot	12		
	AA	Occurrence	%	
	Q	2	16.7	16.7
	A	2	16.7	33.3
	R	1	8.3	41.7
	S	1	8.3	50.0
	K	1	8.3	58.3

(2)

G8	Ntot	66		
	AA	Occurrence	%	
	Q	10	15.2	15.2
	R	8	12.1	27.3
	E	7	10.6	37.9
	I	7	10.6	48.5
	K	6	9.1	57.6

C4	Ntot	24		
	AA	Occurrence	%	
	K	3	12.5	12.5
	E	3	12.5	25.0
	F	3	12.5	37.5
	Q	2	8.3	45.8
	S	2	8.3	54.2

(3)

D7	Ntot	18		
	AA	Occurrence	%	
	A	3	16.7	16.7
	K	3	16.7	33.3
	R	3	16.7	50.0
	T	3	16.7	66.7

F2	Ntot	12		
	AA	Occurrence	%	
	S	3	25.0	25.0
	K	2	16.7	41.7
	T	2	16.7	58.3

(4)

D5	Ntot	42		
	AA	Occurrence	%	
	S	6	14.3	14.3
	A	6	14.3	28.6
	L	4	9.5	38.1
	Y	4	9.5	47.6
	N	4	9.5	57.1

c

Terminal-0	Ntot	108		
	AA	Occurrence	%	Cumul %
	K	14	13.0	13.0
	A	13	12.0	25.0
	R	12	11.1	36.1
	N	10	9.3	45.4
	S	9	8.3	53.7

Terminal-1	Ntot	66		
	AA	Occurrenc	%	Cumul %
	Q	9	13.6	13.6
	K	8	12.1	25.8
	S	7	10.6	36.4
	R	6	9.1	45.5
	L	6	9.1	54.5

Terminal-2	Ntot	36		
	AA	Occurrenc	%	Cumul %
	Q	5	13.9	13.9
	A	5	13.9	27.8
	S	4	11.1	38.9
	E	4	11.1	50.0
	T	4	11.1	61.1

Terminal-3	Ntot	30		
	AA	Occurrenc	%	Cumul %
	S	5	16.7	16.7
	R	5	16.7	33.3
	Q	3	10.0	43.3
	L	3	10.0	53.3

Terminal-4	Ntot	12		
	AA	Occurrenc	%	Cumul %
	Q	3	25.0	25.0
	S	2	16.7	41.7
	R	2	16.7	58.3

Figure S1d. Amino acid (AA) occurrence analysis of the hypervariable positions in selected proteins. (a) Global occurrence for the entire set of 9 selected proteins totaling 43 repeats. (b) Occurrence for each protein. Online the most frequent AA up to a cumulative occurrence exceeding 50% are shown. (c) Occurrence per repeat indexed from the terminal repeats. Online the most frequent AA up to a cumulative occurrence exceeding 50% are shown.

The sequences of the nine selected proteins are analysed in Figure 1c. The global occurrence (Figure S1d (a)) shows that the five most frequent amino acid (AA) in hypervariable positions are Glutamate, Arginine, Lysine, Serine and Alanine, which represent, in total, more than 50% of the occurrences.

When each selected protein sequence is analysed separately, as displayed in Figure S1d (b) Gln-Arg-Lys-Ser are the four most frequent AA for four proteins, A12, F5, F9 and F10. Three of these AA along with glutamic acid are the most frequent for proteins G8 and C4. Two of these AA along with Threonine are the most frequent for proteins D7 and F2. Finally, Serine is also the most frequent AA for D5.

When each repeat, starting from the terminal repeat, is considered separately, as shown in Figure S1d (c), the globally most frequent amide (Gln, Asn), amine (Arg, Lys) and hydroxyl/carboxy (Ser, Glu, Thr) AA are found to be evenly distributed across the hypervariable surface.

S2. Determination of Au(111)-binding affinity of selected αRep by SPR

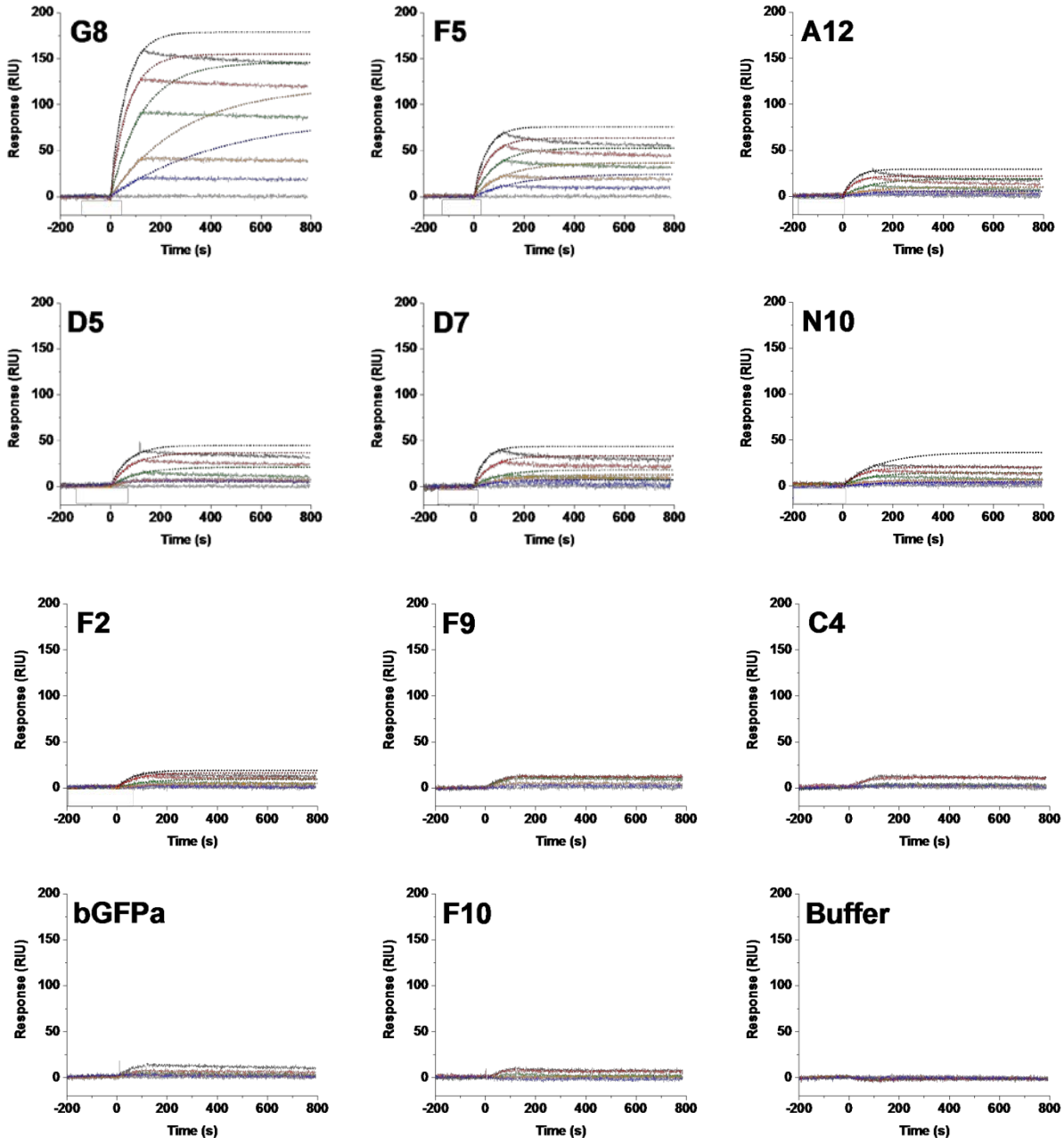

Figure S2a. SPR sensogram overlays showing interaction of immobilised αRep proteins with citrate-stabilised 5-nm Au nanospheres at concentrations of 10 nM (black), 5 nM (red), 2.5 nM(green), 1.25 nM (orange), 0.625 nM (navy blue) and 0 nM (grey). The dotted line shows the fit of the data to a 1:1 Langmuir binding model (for the association phase only). A flow rate of 100 µl/min was used.

The SPR based optical biosensor, ProteOn XPR36 (Bio-rad), was used to determine the affinity and binding kinetics of αRep's interaction to gold nanoparticle surface. In a typical experiment, 200 RU of histidine-tagged αRep protein are immobilized onto tris-NTA/Ni sensor chip in 10 mM phosphate buffer to obtain a homogeneous ligand surface. Nonspecific adsorption during immobilization process is blocked by adding 0.005% Tween 20 to the phosphate buffer. This reliable binding through the flexible His-tag located at one end of the protein obviates the risk of protein damage upon immobilization. Unlike other covalent coupling chemistry (e.g. NHS/EDC),

this method does not chemically modify the active surface of the proteins. Additionally, the Ni/NTA-His-tag protocol allows to immobilize all proteins in the same way without additional complexities, such as variability of exposed binding sites due to the heterogeneity of covalent grafting and the lack of control of the orientation of the proteins once grafted on the sensor surfaces. Next, interaction with gold nanoparticles (Au_{cit}) is measured at 100 µl/min to avoid mass transport effects. 10-nm gold NP are known to be essentially penta-twinned, thus exposing accessible (111) surfaces.[4] At 100 µl/min flow, the initial on-rate is maximum. Flow is allowed to occur for several seconds to establish a baseline, and then various concentrations of gold nanospheres (10, 5, 2.5, 1.25 and 0.625nM) are injected. The association is followed for 120 seconds, after which the gold nanoparticle sample is replaced with 10 mM phosphate buffer, and the dissociation of the αRep / Au_{cit} complex is monitored for 600 seconds. We have designed the "inverted" SPR experiments described above where the binding protein is immobilized on a passivated classical SPR sensor chip because there are no available SPR sensor chip made from gold surfaces with controlled (111)-terminated surfaces over which we could have flown solutions of our selected proteins as in standard SPR protocols. We have conducted a number of such SPR experiments using exactly this type of "inverted" sensor chips.[5] The immobilized α-Rep are invariably functional and their behavior match the results of complementary methods such as crystallographic data.

Detailed SPR data analysis

Figure S2a demonstrates the steady-state response at different concentrations of injected gold nanoparticles (Au_{cit}) over the surface-immobilized αRep. The association (resp. dissociation) phases are clearly visible on all the sensograms, R(t), and more quantitative insight can be gained by analysing them with the model described by Equation (1) (resp. Equation (2)):

$$R(t) = R_{eq}\left(1 - e^{-\left(k_{on}[Au_{cit}]+k_{off}\right).t}\right), \text{ for } 0 \leq t \leq t1 \quad (1)$$

$$R(t) = R_{\infty} + (R_1 - R_{\infty})e^{-k_{off}.(t-t_1)}, \text{ for } t \geq t1 \quad (2)$$

$$K_D = \frac{k_{off}}{k_{on}} \quad (3)$$

where R_{eq} and R_{∞} are the asymptotic equilibrium values of the association and dissociation phases respectively. t_1 and R_1 are the time and SPR signal at the onset of the dissociation phase. k_{on} and k_{off} are the kinetic constants associated with the nanoparticle-protein binding equilibrium.

The fits to the association phase of the experimental data using equation (1) are displayed as continuous black lines in Figure 2a and were repeated for concentrations of gold nanoparticles, [Au_{cit}], ranging from 1 to 10 nM (Fig. S2a). This kinetic analysis of the association phase shows the linear variation of the exponential factor with [Au_{cit}], $k = k_{on}.[Au_{cit}]+k_{off}$, from which k_{on} and k_{off} are extracted (Fig. S2b). These kinetic constants are given in Figure 2d along with a first estimate of the affinity constants K_D#1 calculated from equation (3).

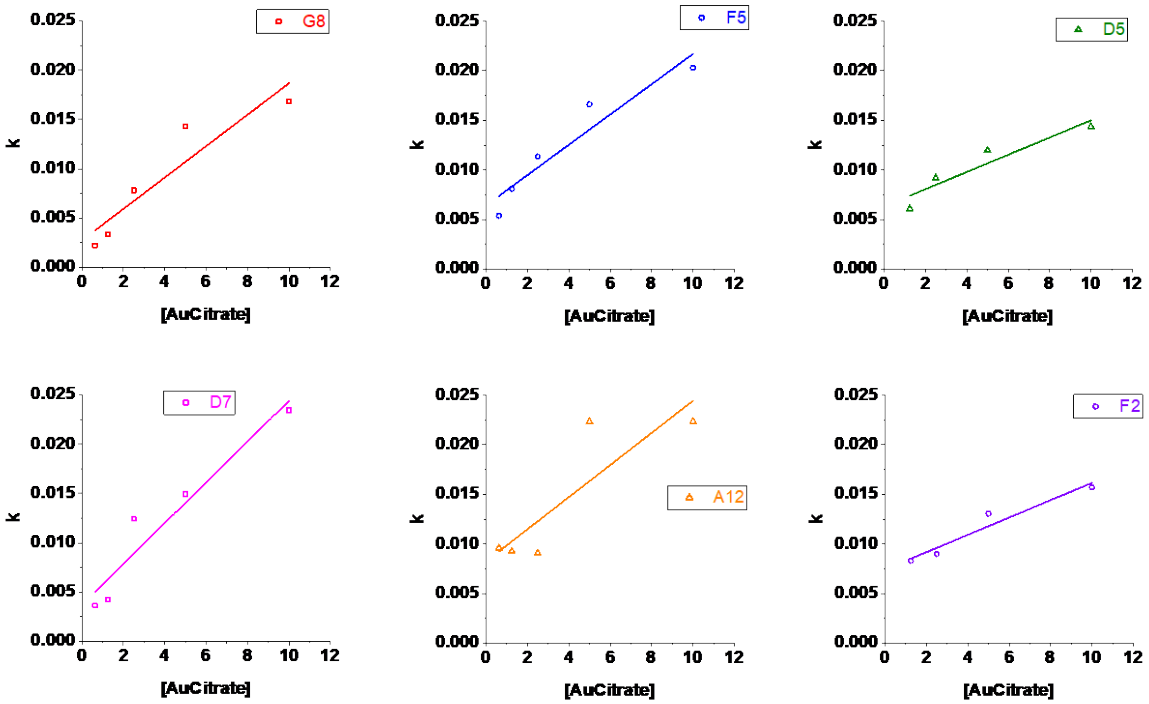

Figure S2b. Linear analysis of k Vs [Au_{cit}] plots obtained for 6 different αRep's.

However, several reasons such as mass transport limitation, steric hindrance or negative cooperativity between binding sites or analyte multivalence have been invoked for the plateauing, in the k vs [Au_{cit}], which underestimates k_{on} and may overestimate $k_{off.}$ [6-9] Both deviations result in a net overestimate of the equilibrium constant. All contribute to an over-estimate of K_D#1.

Alternatively, by assuming that the dissociation phase relates to the same equilibrium between the bound proteins and the dispersed nanoparticles as the association phase, a second and more accurate estimate of the dissociation kinetic constant, k_{off} #2, can be obtained by fitting the decrease of SPR signal after t_1 with equation (2), as shown in Fig. S2c and also overlaid in black lines in Fig. 2a for $t \geq 120$ s.

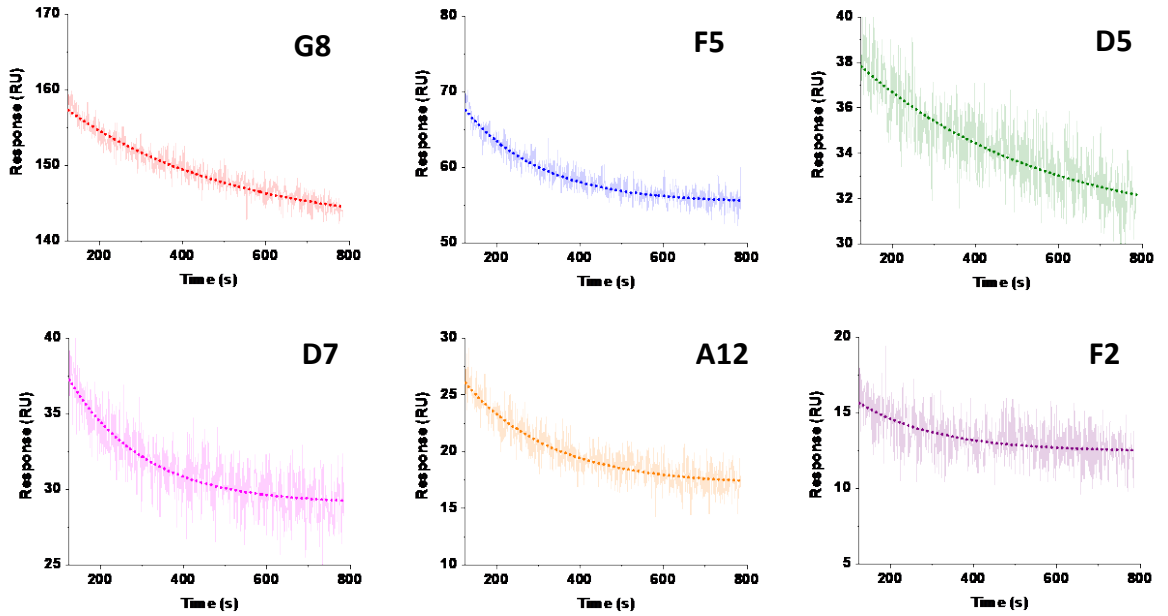

Figure S2c. Exponential decay fits on sensograms obtained upon buffer induced dissociation of loosely bound αRep gold nanoparticle complex pairs at 10nM [Aucit] using the fully explicit Eq. (2). R_1 is known experimentally, only 2 fitting parameters are used: SPR_∞ and k_{off} #2.

Figure S2c illustrates exponential decay fits for desorption phase of gold nanoparticles from the homogeneous ligand surface composed of any of the 5 selected αRep: G8, F5, D5, D7 and A12. Note that, within the time frame of the experiments, we observe that the dissociation phase tends towards an asymptotic constant value which indicates that the rinsing step leaves a finite amount of bound proteins. This observation is accounted for by the constant term R_∞ in equation (2). Values of k_{off}#2 and R_∞ (asymptotic value at infinite time) are obtained from the fits using equation (2) whereas R_1 is determined directly from raw data.

To further validate the reliability of k_{off} #2 values obtained through exponential decay fits, a new equation (5) was derived as follows:

Equation (2) can be re-written as:

$$\frac{R_t - R_\infty}{R_1 - R_\infty} = e^{-k_{off}*(t-t_1)} \quad \text{.....Eq (4)}$$

Taking logarithm on both sides, and writing $x = (t-t_1)\ t$

$$ln\left[\frac{R_t - R_\infty}{R_1 - R_\infty}\right] = -k_{off} * x \quad \text{.....Eq (5)}$$

Figure S2d replots the same data and fits as Fig. S2c but in the new coordinate system. The experimental plots in Fig. S2d are indeed linear which confirms the single exponential decay with a constant k_{off} #2 that can be computed from the slope of the linear fits and are tabulated in Table1 along with empirically derived R_∞ and pre-determined R_1 values. Of course such plots are much more sensitive as it amplifies the noise but also provides a more reliable uncertainty values.

The non-zero value of R_∞ suggests that not all αRep complexed gold nanoparticles leave the surface at infinite time. A similar trend has been reported in studies conducted on several related interacting systems.[8,10]

We note that we cannot fully exclude that this dissociation equilibrium might be related to a different set of species than the association phase, including modified proteins that may undergo an irreversible binding mechanism. Yet, in the absence of experimental evidence of such a case, we hypothesized that both phases were related to the same equilibrium.

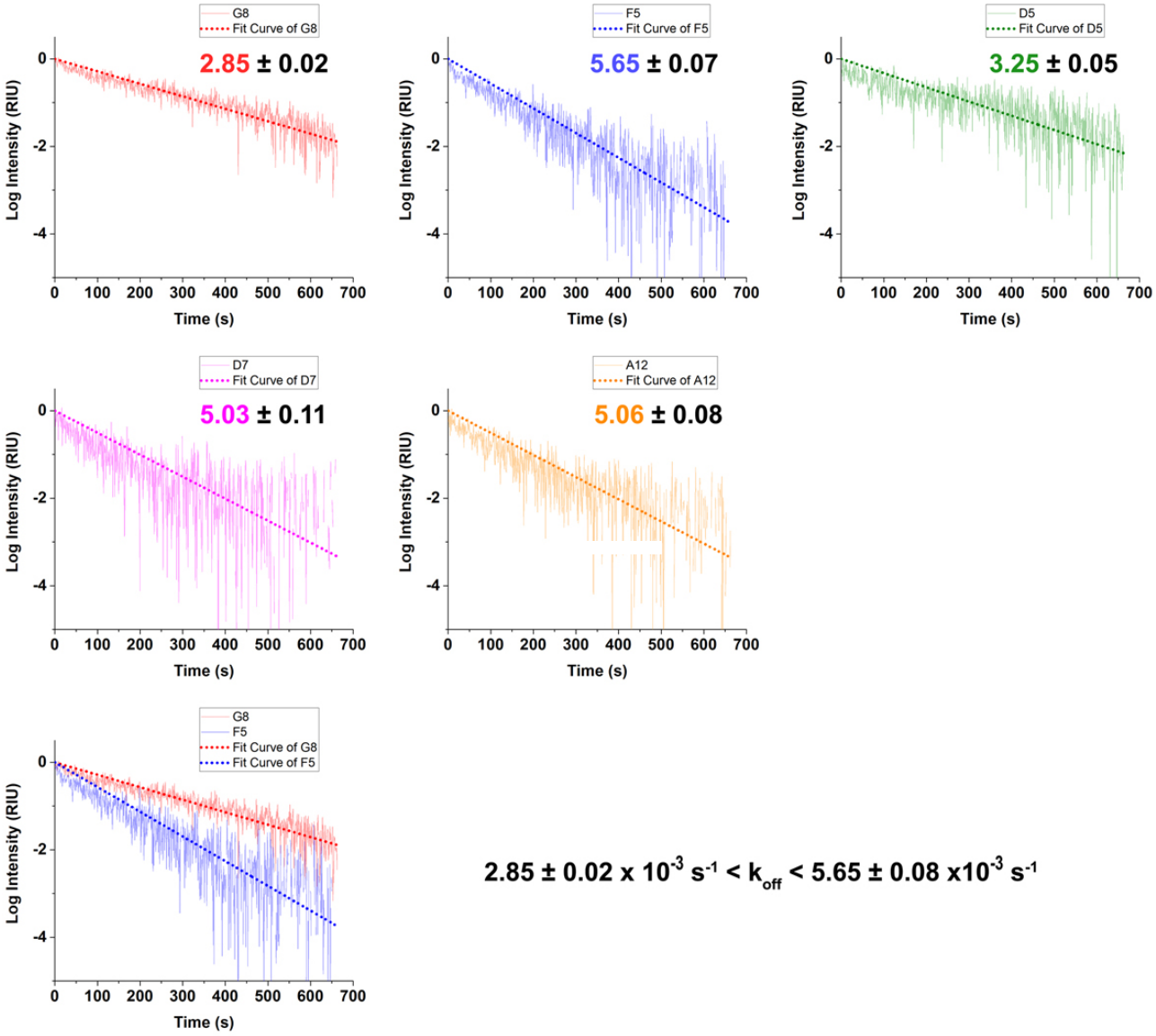

Figure S2d. Replots of dissociation phase. Linear fits to the logarithm of the normalized 10nM SPR data vs time as described by equations (4) and (5). The intercept is 0 and the slope gives the k_{off} #2values. The two extreme cases, G8 and F5, are replotted together in the last panel; all other data fall in between.

The k_{off} #2 are comprised between $2.85\pm0.02\text{x}10^{-3}$ s^{-1} (G8) and $5.65\pm0.08\text{x}10^{-3}$ s^{-1} (F5), i.e. almost systematically lower than k_{off} #1 as expected due to the plateauing in k vs [Au_{Cit}] plots (Fig. S2b). This corrected set of equilibrium dissociation constants, $K_D\#2 = (k_{off}\#2)/k_{on}$, ranges from ca. 2 to 6 nM and essentially preserves the affinity ranking with G8 the strongest and D5 the weakest binders.

Immobilised protein	R_1	R_∞	k_{off} #2 ($10^{-3}s^{-1}$)
G8	159.3	141.4	2.85 ± 0.02
F5	70.6	55.3	5.65 ± 0.07
D5	40.5	30.6	3.25 ± 0.05
D7	39.2	29.0	5.03 ± 0.11
A12	28.7	17.1	5.06 ± 0.08

Table 2: Empirical values for R_1 and fitting parameters SPR_∞ and k_{off} #2 of the dissociation phase of αRep gold nanoparticle complex for 6 selected αRep's (obtained using Eq 4).

Finally, the quality and sensitivity of the fits on the association phase provides reliable asymptotic equilibrium SPR values, R_{eq}, which are fitted by the Langmuir isotherm model in Figure 2b and processed using the Scatchard method in Figure 2c. The linearity of the Scatchard plots validates this approach and a third dataset in Table 2d, K_D#3, is obtained from the slopes of the linear fits and ranges from 0.71 ± 0.06, for G8, to 5.10 ± 0.80, for D5.
The third approach determines the equilibrium dissociation constant directly from Scatchard plot[11] using equation (6) without measuring the kinetic constants (k_{on} and k_{off}).

$$R_{eq} = \frac{R_{eq}}{[Au_{cit}]} \times (-K_D) + R_{max} \quad \text{Eq (6)}$$

With this plot, K_D values can be obtained from the slope of the linear fits in the R_{eq} Vs $R_{eq}/[Au_{cit}]$ graph. The K_D#3 values obtained from Scatchard plot are summarized in the table of Fig. 2d in the main text and agrees well with the K_D#1 and K_D#2 affinity values considering the limitations of each approach.

S3. TEM and agarose Gel Electrophoresis on αRep-capped Au seeds

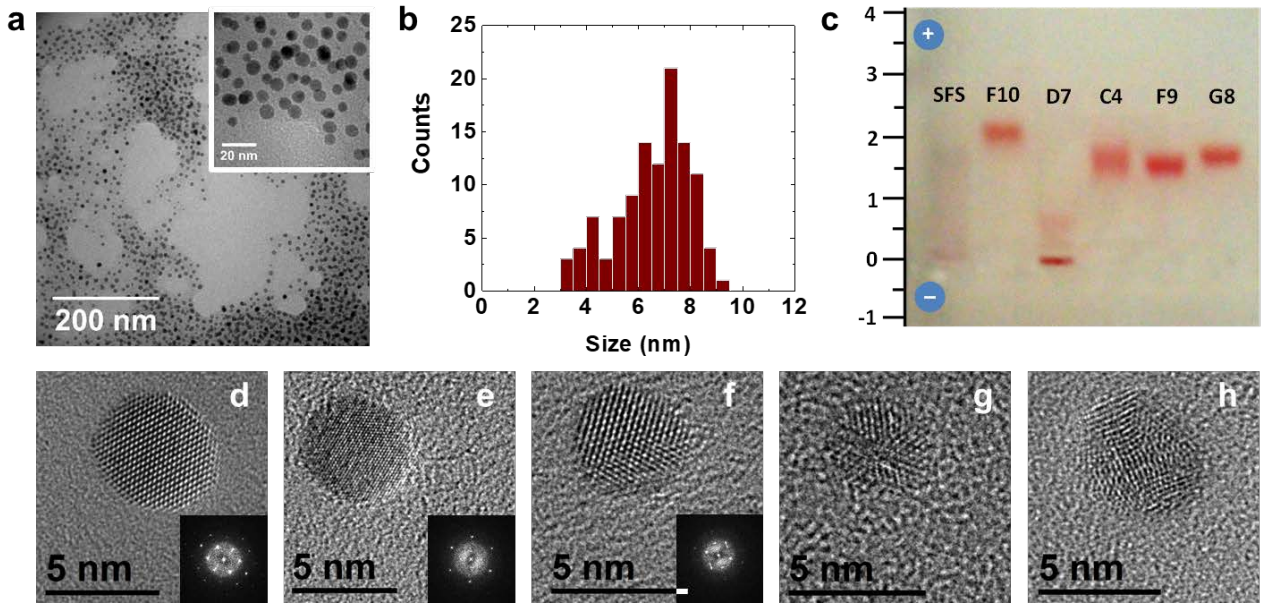

Figure S3. Structural characterisation of αRep capped Au seeds. (a-b) A typical TEM micrograph of G8 capped seeds demonstrating the presence of small nanoparticles with an average size distribution of 6±2 nm. (c) Agarose gel electrophoresis showing mobility of Au seeds produced in the absence (leftmost lane labelled "SFS") and presence of 5 different Au(111) selected αRep proteins: F10, D7,C4,F9 and G8 (from left to right). Seeds with F10, C4, F9 and G8 are negatively charged, D7 is neutral whereas SFS (uncapped) exhibit negative surface charge but smear out in electrophoresis buffer (0.5X Tris-Borate-EDTA, pH~8.5). (d-h) High resolution TEM of (d, e) monocrystalline along the [011] and [111] zone axis respectively, (c) single twinned, (d) pentatwinned and (e) polycrystalline seeds. The insets in (d), (e), (f) are electron diffraction patterns of the corresponding seeds.

The αRep templated Au seeds are produced by the direct reduction of Au^{3+} to Au^{0} state with sodium formaldehyde sulfoxylate (SFS, as described in Methods Section A). Figure S3 shows the characterisation of these seeds by conventional and high resolution transmission electron microscopy (TEM) and agarose gel electrophoresis. The αRep capped seeds show a wide size distribution with an average of 6 ± 2 nm (Figure S3b).

To determine the stability and electrophoretic mobility of αRep templated Au seeds, gel electrophoresis is performed in 0.3 w/v% agarose gel. Seeds prepared with 5 different Au(111)-selected αRep: F10 (lane 2), D7 (lane 3), C4 (lane 4), F9 (lane 5) and G8 (lane 6) are tested against non-templated pure SFS-Au seeds (lane 1). All seeds except those prepared with D7, migrate towards the positive electrode terminal forming distinct bands. Non-templated seeds also migrated towards positive end but generated a smeared pattern instead of a clear band suggesting their lack of stability. D7 capped seeds is electrically neutral at pH 8.5 (pI= 8.4) and consistently demonstrates no appreciable mobility in the gel.

The detailed crystalline structure of the seeds has been investigated by high resolution TEM. Typical representatives are shown in Figures S3(d-h). Monocrystalline, single and pentatwinned as well as polycrystalline seeds can be found without prevalence of any of these structure. It is unlikely that the final morphology and structure of the nanocrystals are determined by the seeds at this stage but rather later on as their size reaches 10-15 nm. Note that all seeds are spherical irrespective of their crystalline structure, which reinforces the simple capping role of the proteins at the seed stage rather than a facet-specific growth inhibition which is engaged at a later stage when the crystals are larger.

S4. Two-stage seeded growth approach for morphosynthesis

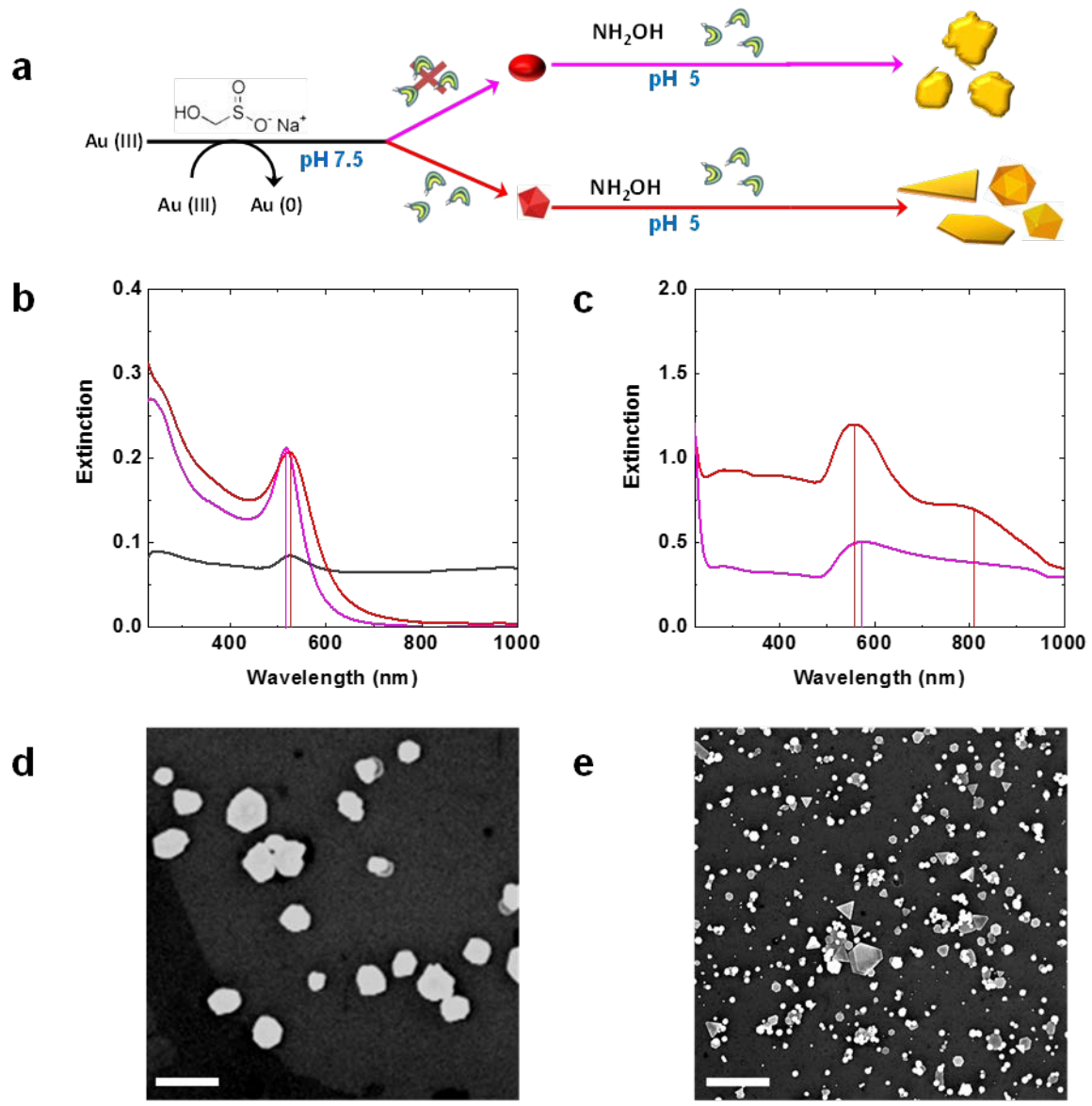

Figure S4. Comparative analysis of seeded growth method without and with αRep.(a) Schematic representation of seed synthesis and growth stage of Au morphosynthesis effectuated by reducing agents SFS and Hydroxylamine respectively. UV-Vis characterisation of (b) Au seeds produced by reducing Au^{3+} with SFS in (i) absence of αRep in pH 7.5 adjusted water (pink) and 50 mM phosphate buffer(grey) (ii) presence of αRep in 50 mM phosphate buffer (red) (c) Au nanocrystals resulting from the hydroxylamine initiated selective reduction of Au^{3+} onto αRep deprived seeds (pink) and αRep capped seeds (red) in growth solutions supplemented with 4μM αRep. Morphological characterisation of Au nanocrystals obtained upon hydroxylamine mediated growth of (d) αRep deprived seeds and (e) αRep capped seeds. Scale bars 500 nm.

Seeded growth approach has been widely used to synthesise monodisperse metallic nanoparticles, where a concerted action of reducing and capping agents is vital in guiding the crystal structure.[12] In our approach, Au seeds are first produced by reduction of $HAuCL_4$ with sodium formaldehyde sulfoxylate (SFS) at pH 7.5. The selective reduction of Au^{3+} on Au seeds is then initiated by hydroxylamine under mild acidic condition (pH 5.0) to give rise to faceted nanocrystals. As schematically illustrated in Figure S4a, the exclusion of capping agent (αRep) at the seed stage can abruptly disorient the crystal growth process. For a detailed inspection, spectroscopic and structural characterisation of colloids are performed at the end of seed and growth stages. As evident in Figure

S4b, SFS-reduced Au seeds (λ_{res} = 517 nm) maintain colloidal stability in water adjusted to pH 7.5 but destabilise in ionic buffer (shown in grey lines). When Au binding αRep proteins are added to the same reaction medium, the seeds demonstrate excellent stability (λ_{res} = 524 nm). While some spectroscopic resemblance is present at the seed stage, the spectra after hydroxylamine seeding demonstrates obvious differences, which stems from the crystallography of seeds. Nanocrystals emerging from αRep capped Au seeds exhibit two distinct resonance peaks at 556 nm and 804 nm in the UV-Vis spectrum(Figure S4c), which translates into the presence of pseudo-spherical shapes (including icosahedrons and decahedrons) and platonic structures respectively (Figure S4e). Au seeds grown in the absence of added αRep are devoid of these characteristics and instead show a broad peak at 576 nm which results from 0.2-1.0 µm irregular/pseudo-spherical nanostructures (Figure S4d)

S5. SEM characterization of Au nanocrystals synthesized in the presence of Au(111)-selected αRep.

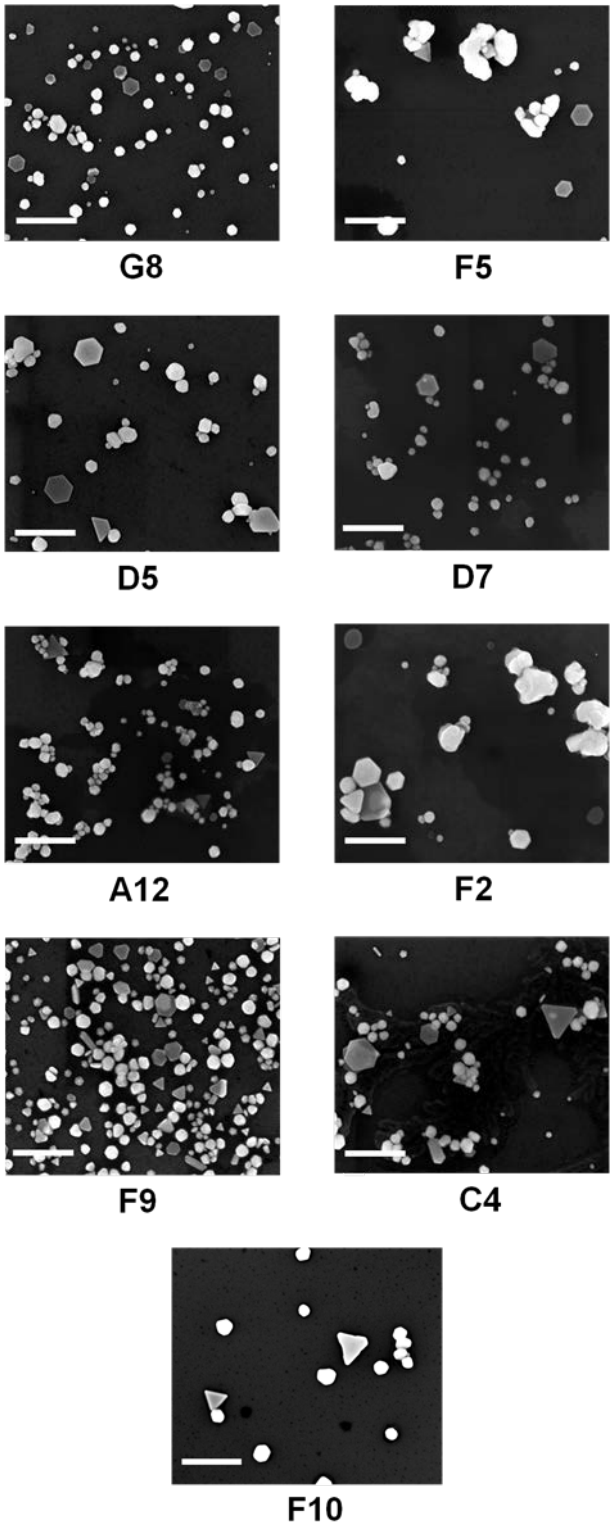

Figure S5. SEM micrographs of 9 different Au nanocrystal batches synthesized in the presence of one particular Au(111)-selected αRep protein indicated by the label.(Scale bar: 500 nm)

The influential role of the Au(111)-selected αRep during the growth of the Au nanocrystals is illustrated in Figure S5. All selected proteins are able to produce platonic and pseudo-spherical nanostructures under experimental conditions. However, subtle efficiency differences in morphosynthesis can be observed and correlated to SPR affinity signals, which allows categorising these proteins into three subgroups.

Group I.
It includes **G8**, **D5** and **F9**, which all have a pI lower than 7. These proteins lead to colloidally stable nanocrystals (nanoplates, icosahedra and decahedra particles) alongside a small fraction of irregular shapes. In these acidic αRep proteins, no statistic enrichment of the variable position is observed, except for a slight reduction of lysine in favor of glutamic acid,. Interestingly, these proteins are the longest ones (n = 6, 7, 10) but the protein length does not account for their morphosynthetic activity as N10 (See section S7) and G8 have the same number of internal repeat without sharing the surface specificity.

Group II
Contains proteins with a few internal repeats (n=1, 2 or 3) such as **C4**, **F10** and **A12**, **D7**. The pI is lower than 7 for the former two and higher than 7 for the latter two. The former two give a low SPR signal while the latter two show a significant affinity for citrate-stabilized Au nanoparticles, which could be enhanced by attractive electrostatic interactions even if the specific affinity for the Au surface were moderate. This group of proteins is almost as capable as Group I in giving rise to (111)-faceted nanostructures, but the nanocrystals tend to coalesce after synthesis. This suggests the inability of these low molecular weight ligands to effectively stabilize the submicron-sized objects in buffered medium either because of their close-to-neutrality pH or their relatively weaker chemisorption that forces them to quit the nanocrystal surface after synthesis.

Group III
F2 and **F5** are single internal repeat proteins with high pI, which produce only a small fraction of large Au(111) faceted nanoparticles. Among large structures, ill-shaped ones are more prominent and colloidal aggregation occurs readily. Those two binders present similar size, pI and morphosynthesis properties. The phage display procedure on (111)-terraced Au substrates does not exclude the selection of very short gold-binding proteins that were electrostatically or even non specifically attached on locations exposing facets with different orientations.

Finally, it appears that the 9 selected proteins might not have been isolated for the same type of interactions with the substrate, which would explain why the sequence analysis does not show well defined trends. Group I and C4, F10 appear to be genuine and specific Au(111) binders with the morphosynthetic performances of the latter two slightly hampered by their small size. Group III and A12, D7 are strong electrostatic Au binders with less prominent (111) crystal facet specificity.

S6. Spectral characterization of Au nanocrystals synthesized in the presence of Au(111)-selected αRep.

Au nanocrystals synthesized with one αRep templates (A12, C4, D7, F2, F5, F9, F10 or G8) are characterized by UV-Visible spectroscopy (Cary-5000 UV−vis NIR spectrophotometer).

As depicted in Figure S6, well-defined plasmon resonance peaks for pseudospherical and platonic nanostructures (~530 nm) are observed in the spectra of Group I (G8, F9) and II (C4, D7, F10). Other nanocrystal batches produced with low internal repeat αRep (A12 and Group III) exhibit lower absorbance and broader spectra in the UV-vis region which is essentially attributed to nanoparticle aggregation due to lack of colloidal stabilization by close-to-neutral protein coating, but could also be explained by a lower concentration of nanoparticles and concomitant increase in nanoparticle size due to limited nucleation in the growth medium.

Spectra for G8, F9 and C4 also present the shoulder at 750-800 nm that is attributed to higher order plasmon mode in submicron nanoplates.

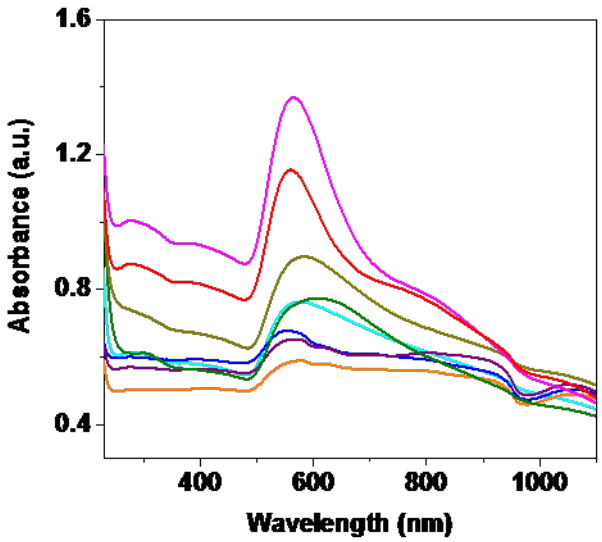

Figure S6. UV-Vis spectra of as-synthesized Au nanocrystal batches obtained using one of the Au(111)-selected αRep protein: F10 (cyan), A12 (blue), F2 (purple), F5 (orange), D7 (olive), C4 (dark yellow), F9 (pink) and G8 (red).

S7. Control experiments with non-selected αRep's

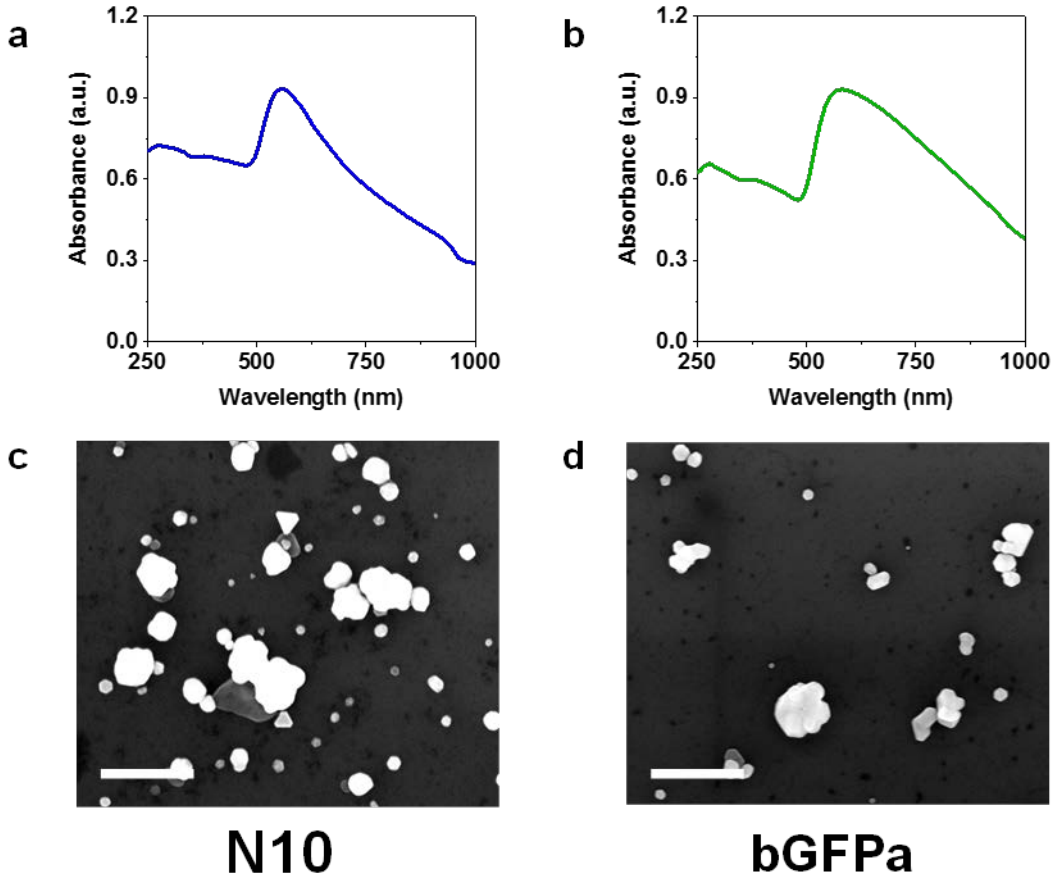

Figure S7. (a,b) UV-visible and (c,d) SEM characterization of Au nanostructures formed by the templating action of non-selected αRep proteins. (a,c) N10 is a non-selected, consensus sequence αRep protein with no specific affinity properties that shows some Au nanoparticle reduction activity but no morphological control (positive control). (b,d) αRep bGFPa was selected against green fluorescent protein (GFP) and so underwent the phage display procedure but similarly lead to the production of shapeless Au nanoparticles(negative control). SEM Scale bar: 500 nm.

Positive and negative controls were performed using non-selected αRep N10 and anti-GFP selected bGFPa respectively, to assess the critical role of Au(111) facet binding selection for αRep to acquire the capability to control the morphosynthesis of facetted gold nanocrystals. UV-visible spectra of control samples prepared in the presence of N10 and bGFPa proteins (Figure S9a-b) shows a peak for pseudospherical structures (λ_{abs}~ 540 nm), but lacks the characteristic peak for platonic nanostructures. A detailed analysis with scanning electron microscopy further confirms that indeed both N10 and bGFPa gives rise to majority of complex-shaped nanoparticles (> 75%) when included in the seeded-growth medium (Figure S9a-d). This strongly demonstrates that only facet selective αRep proteins promote the growth of Au (111) terminated Au nanocrystals.

S8. Au nanocrystal size tunability during αRep-controlled morphosynthesis.

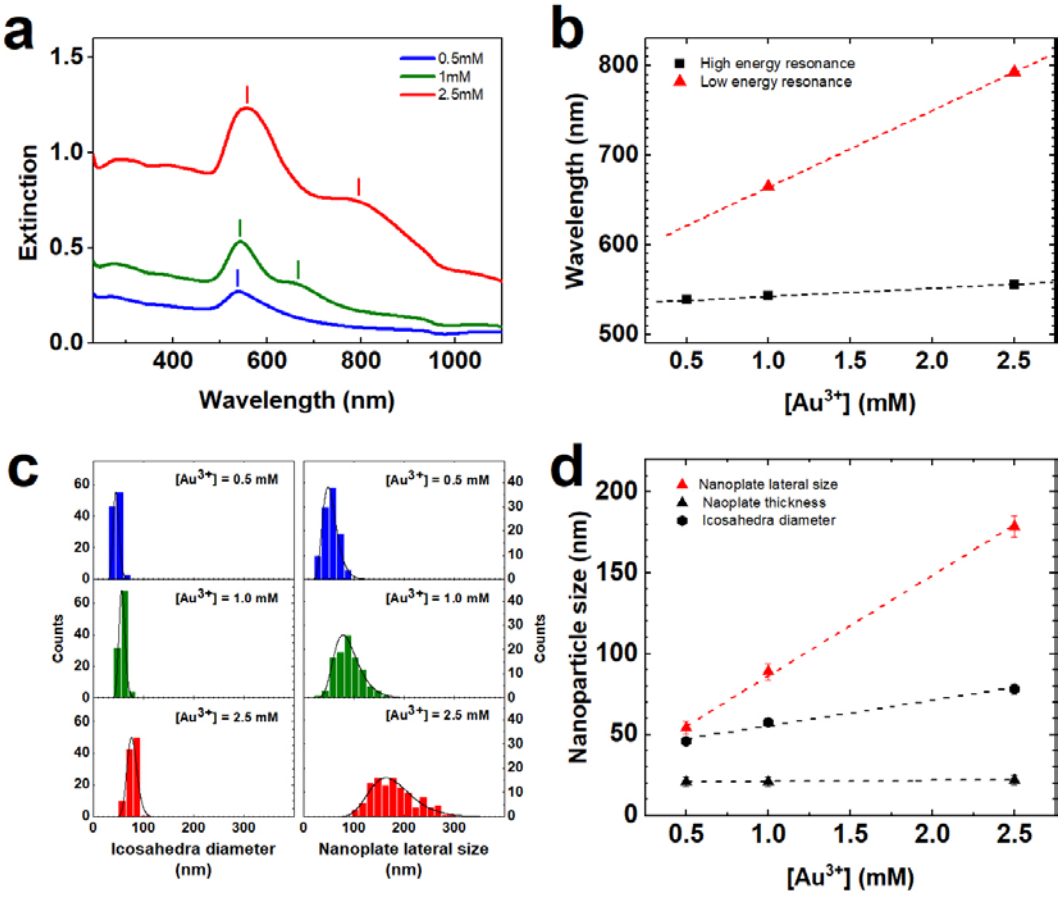

Figure S8. (a) UV-Vis spectroscopy of Au nanocrystals synthesized with 3 different Au^{3+}concentrations: 0.5 mM (black), 1.0 mM (blue) and 2.5 mM (red). A progressive increase in absorbance intensity and red shift in resonance position is observed as the Au^{3+}concentration increases indicating increase in particle size. Distinct in-plane higher order modes mode of anisotropic gold nanoplates becomes evident in the spectra at and above [Au^{3+}] of 1mM (indicated by the second vertical marker above 600 nm). (b) Evolution of the energy of the plasmon resonances with [Au^{3+}]. The transverse mode is plotted in black and the approximate central energy of the higher order modes is plotted in red. **(c)** Particle size lognormal distributions as a function of initial [Au^{3+}] (0.5, 1.0 and 2.5 mM) for icosahedra (diameter) and plate (lateral size). **(d)** Evolution of the mean lateral size of the plates (red triangle) and their thickness (black triangles) and of the icosahedra diameter (black circles).

αRep capped Au seeds were injected into growth solutions containing different initial Au^{3+}concentrations along with hydroxylamine and free αRep proteins as described in the Experimental sections of the main text and Section A of this document. The pH for each growth solution was set to 5.5.

A first step is indicated by the solution colour changing to greyish blue which takes 15 min for [Au^{3+}]=0.5 mM, almost 10-12 min for [Au^{3+}]=1 mM and 2-3 min for [Au^{3+}]=2.5 mM. This initial, diffusion limited step corresponds to the partial reduction of the bulk Au(III) into Au(I) by the hydroxylamine.

In a second step, the autocatalytic disproportionation occurs where Au(I) reaches the solid Au(0) surface where it is reduced and contributes to the nanocrystal growth. This Au(I) adsorption and autocatalysis is the limiting step, therefore the "rate of crystallization" does not vary with the initial [Au^{3+}]. Indeed, we observe that the completion time increases as the initial Au(III) concentration is

increased. It is 1 hour for [Au^{3+}]=0.5 mM, 1.5-2.0 hours for [Au^{3+}]=1 mM and 2-3 hours for [Au^{3+}]=2.5 mM. Our data suggest a sublinear dependency of the completion time with the initial [Au^{3+}], which rules out the possibility to have a reaction rate increasing with the initial [Au^{3+}].

The second step leads to purple-coloured solution that are characterized by UV-visible spectrophotometry. Figure S8a shows the extinction spectra of three seeded growths of G8-capped nanocrystals for Au^{3+} concentrations of 0.5 mM, 1 mM and 2.5 mM using the same Au seed volume. At low initial Au^{3+} concentration, a single asymmetrical peak is observed, consistent with spheroidal and nanoplates of similar sizes as shown in Fig. 5a. Once the initial Au^{3+} concentration exceeds 1 mM, two peaks become clearly distinct and are indicated with vertical markers in Figure S8a. The peak centered at around 525-540 nm originates from icosahedrons, decahedrons and the small fraction of pseudo-spherical particles but also from the transverse mode of the nanoplates. This peak barely red-shifts with the increasing Au^{3+} concentration (Fig. S8b, black data) since the evolution of the diameter of spheroidal particles and of the nanoplate thickness is slow. The shoulder peak on the low energy side of the spectra originates from the in-plane higher order modes of the Au nanoplates. As expected, this shoulder shifts more rapidly with increasing Au^{3+} concentration (Fig. S8b, red data) as the in-plane modes are very sensitive to the nanoplate edge length that varies from ca. 50 nm to 200 nm for the considered concentration variation.

This is accompanied by the SEM observation that the final nanoplate edge length becomes significantly larger than the average decahedra/icosahedra diameter. By labelling the data shown in Figures 5b-d, we can determine separately the icosahedra diameter and plate lateral size distributions as a function of initial [Au^{3+}] as shown in the Figure S8c. Clearly the lateral growth of the plates is much faster than the icosahedra diameter expansion and summarized in Figure S8d. If one considers also the almost constant plate thickness obtained from AFM measurements (See, for example, Figs. 3i and 3j) for this [Au^{3+}] range, we have a perfect match with the plasmon bands shift as a function of initial [Au^{3+}] shown in Fig. S8b. The low energy resonance is due to higher order modes along the plate edges and so varies much faster than the high energy band, which is due to the averaged contribution of the isotropic resonance of the icosahedra (and decahedra) and the transverse mode of the plates. Figure S8d thus provides the simple linear scaling law between the mean size of crystals and initial [Au^{3+}].

The action of the proteins is to bind to the (111) surfaces where the reaction rate is significantly reduced leading to the observed shapes, in particular the platelets. The less effective binding to (100) and (110) facets results in a faster growth rate of the platelet sides even in the presence of the proteins. Yet, the K_D are finite, the bound proteins have a non-zero probability to detach (partially or entire) creating an opportunity for the small and labile ions, Au(I), to reach the metallic surface. A protein can later on occupy the empty site. Therefore, a very slow diffusion of Au(I) underneath the protein layer remains possible leading to a much slower yet non-zero thickening of the platelets by reduction of Au(I) onto the basal planes. Similarly, a slow growth of the diameter of the icosahedra and decahedra occurs which may be more pronounced than the plate thickening because of the presence of ridges separating two adjacent (111) facets where the protein binding may be sub-optimal.

S9. Effect of pH on the seeded growth process

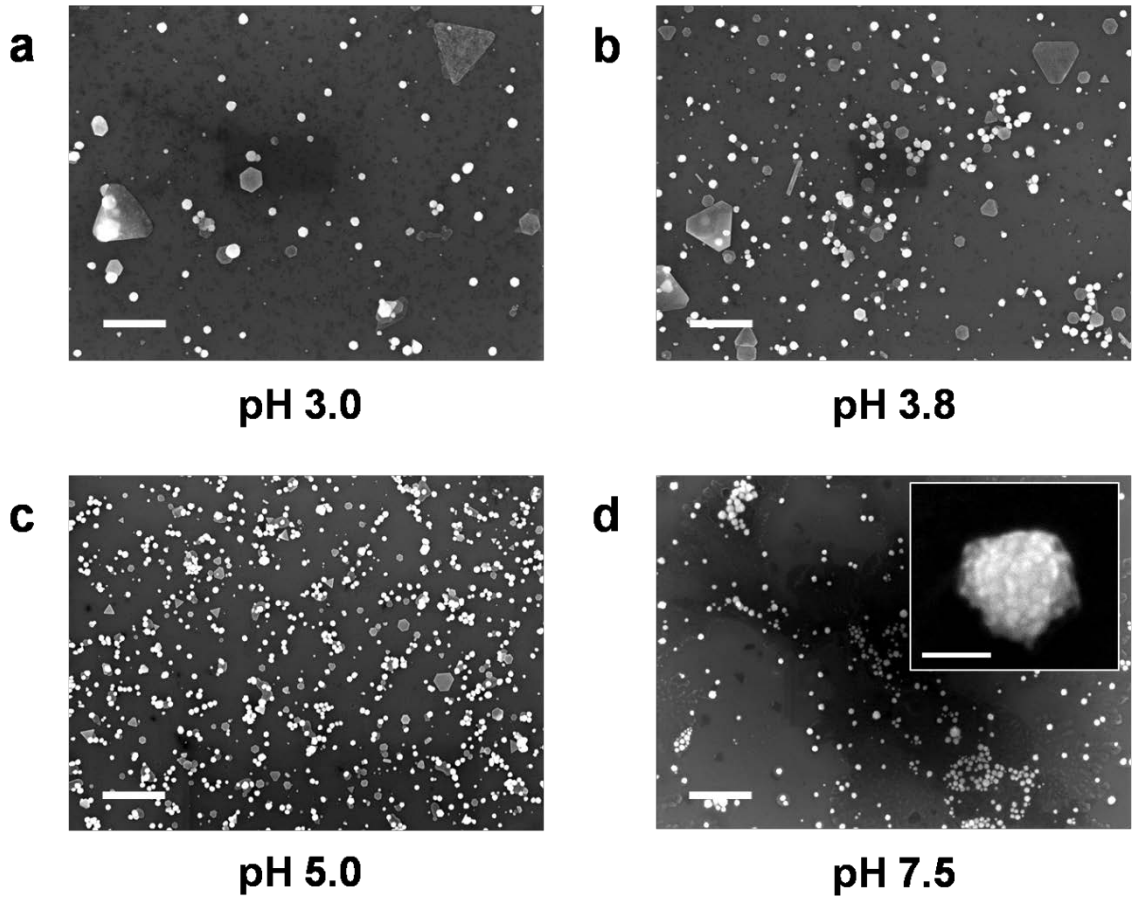

Figure S9. SEM micrographs showing effect of solution pH on the growth process of G8 capped Au nanocrystals. (a-c) Growth occurs on the surface of seeds at pH < 6 resulting in the formation of nanoplates, icosahedrons and decahedrons (d) No growth occurs on seed surface rather hydroxylamine itself directly reduces Au^{3+} to Au^0 at pH > 6 to produce fractal shaped nanoparticles. Scale bars: (a-d) 1µm; d inset 100 nm.

A typical seeded growth method proceeds through the disproportionation reaction,[13] catalysed by the Au seeds (Au_{seeds}/Au_{ion} =+1.68V)[14] in the presence of a weak reducing agent. Previous studies have indicated that all popular reducing agents[15-17] feature a pH- dependent reduction potential and can spontaneously generate new nuclei at basic pH in the absence of seeds.

Therefore, we chose reaction parameters under which secondary nucleation can be suppressed or at least minimized during the growth step. In the present case, hydroxylamine has been used to promote the seeded growth. Hydroxylamine coexists as NH_2OH and NH_3OH^+ in the growth solution (pKa 6.03).[17] At pH > 6, the fraction of the deprotonated form, which has a higher reduction power, increases together with cathodic shift in gold redox potential resulting in the spontaneous reduction of $HAuCl_4$ leading to self-nucleation of irregular dendritic nanostructures.[17] Similar ill-shaped nanostructures are observed in our case at alkaline pH, irrespective of the presence of gold seeds during the growth step (Figure S9). Hence, a pH <5 has been adopted for hydroxylamine seeding method to allow the surface-catalysed reduction of $HAuCl_4$ to take place and suppress any parasitic nanoparticle nucleation and growth. Figure S9 indicates formation of platonic and pseudospherical nanocrystals at pH values between 3 and 5. Besides variations in growth rates of plates and pseudospherical populations no additional effect on the morphology of crystalline subpopulations of Au nanocrystals was observed.

S10. Effect of reaction temperature on morphosynthesis

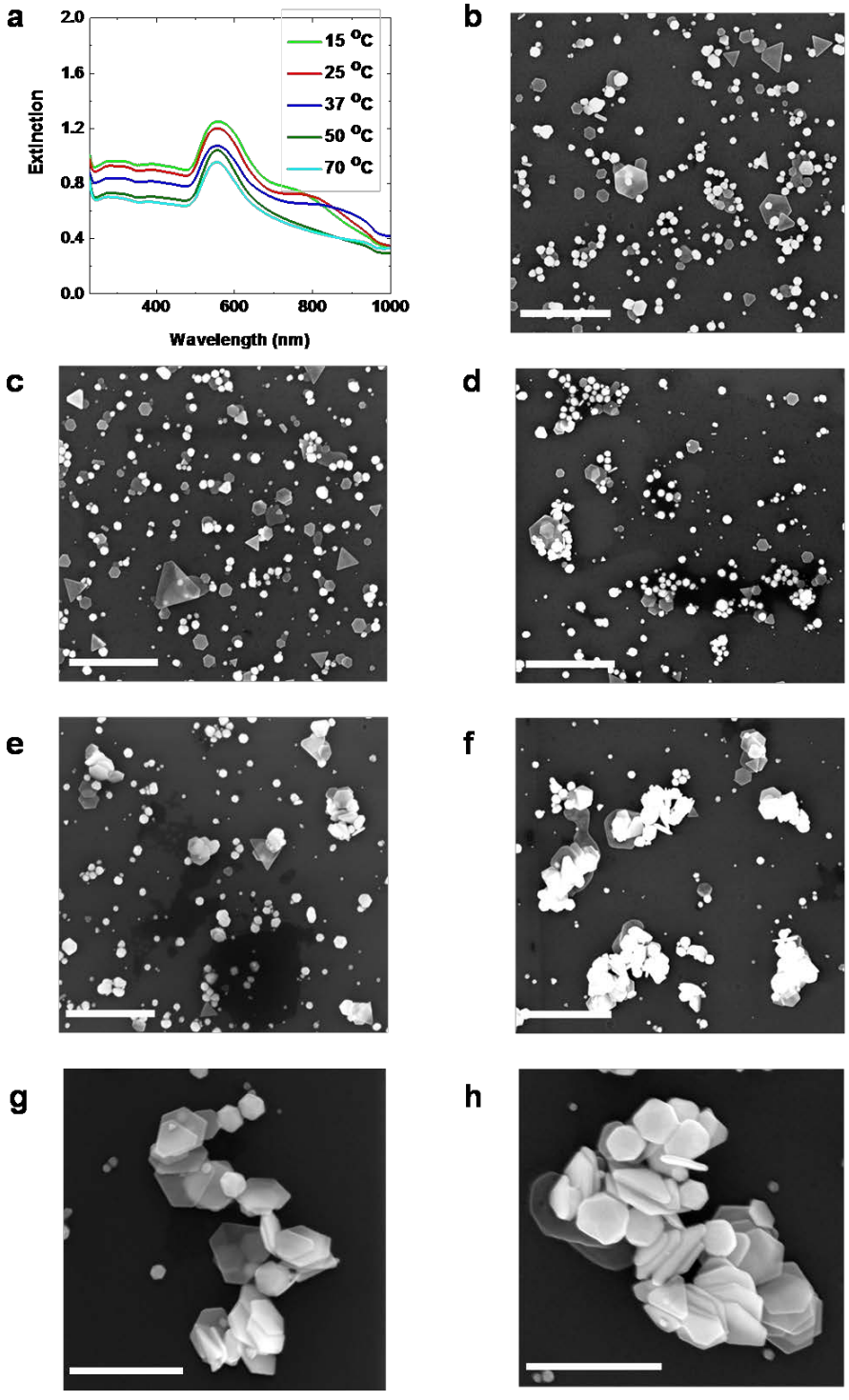

Figure S10. Temperature dependent morphosynthesis of Au nanocrystals at fixed concentrations of Au^{3+} and G8.(a) UV-Vis spectroscopy showing progressive disappearance of in-plane dipole peak of nanocrystal sample at reaction temperatures of 37ºC and above. SEM micrographs of G8 capped nanocrystals at synthesised at temperatures of (b) 15 ºC (c) 25 ºC (d) 37 ºC (e) 50 ºC and (f) 70 ºC. (g-h) Representative images showing high order basal stacking of nanoplates at 70 ºC. (Scale bars: 500 nm)

The growth of gold nanocrystals at 15°C, 25°C, 37°C, 50°C and 70°C, all other parameters being kept identical,are studied to determine the effect of the temperature on the synthesis rate and nanoparticle structure. As shown in Figure S10, and on the contrary to previously reported literature,[18-21] the overall structural composition and yield of the nanocrystal samples remain unaffected even at higher temperatures (50-70°C). In particular, no increase in spherical or shapeless particles is observed. This suggests that the αRep morphosynthetic activity is preserved at high temperatures which allows the formation of Au(111) terminated nanostructures. Interestingly, a slight and gradual increase in nanocrystal size occurs with increase in temperature.

We should note that higher temperatures lead to progressive aggregation of the Au nanocrystals, which eventually leads to disappearance of the characteristic nanoplate 804-nm shoulder in the extinction spectra. The marginal decline in absorbance at 540 nm suggests that pseudospherical structures are less affected by temperature rise. SEM observations show indeed that the nanoplates tend to irreversibly stack together once the synthesis temperature reaches and exceed to 37°C. One possible explanation for this temperature-triggered agglomeration is a partial unfolding although unbound αRep protein have been shown to sustain temperatures as high as 90°C without denaturation. Another possible reason is the establishment of entropically favored protein-protein interactions though side chains.[22] The limited diffusion and surface adsorption of the αRep onto the Au surface when the surface-confined disproportionation reaction rate increases at higher temperatures could also be a factor. Although this would indeed lead to poorly stabilized facets prone to particle-particle flocculation, it is unlikely since the facet growth inhibition is still observed thus certifying that the proteins do interact strongly with the growing facets.

S11. Surface composition of G8-capped nanocrystals

Energy dispersive spectroscopy (EDS) is conducted to study the composition of αRep templated Au nanoparticles (using AMRAY 1820D STEM equipped with EDAX Genesis EDS system). The samples are drop casted onto ultrathin (10 nm) SiO_2 membranes to enable the carbon and nitrogen analysis

The EDS spectrum shown in Figure S11 is obtained when the electron beam is positioned on a single nanoplate and it reveals the predominant presence of Au and Si signals which comes from the nanoparticle surface and the support SiO_2 membrane grid respectively. Additionally, the EDS scan also verify peaks at 0.39 keV and 0.28 keV representing nitrogen (N) and carbon(C) respectively. Nitrogen is considered a strong marker of the protein, which confirms the presence of αRep proteins on the surface of the gold nanoparticles. The experimental element molar ratio of N:C ≈ 5.0, which was quite close to the theoretically predicted values. The excess carbon could be contributed by hydrocarbon contaminants present in the microscope chamber. Elemental presence of oxygen and copper can be attributed to the SiO_2membrane and sample holder or to surface contamination. The sodium, chlorine and calcium signal appears from the buffer systems that has been used during protein extraction, purification and rehydration stages.

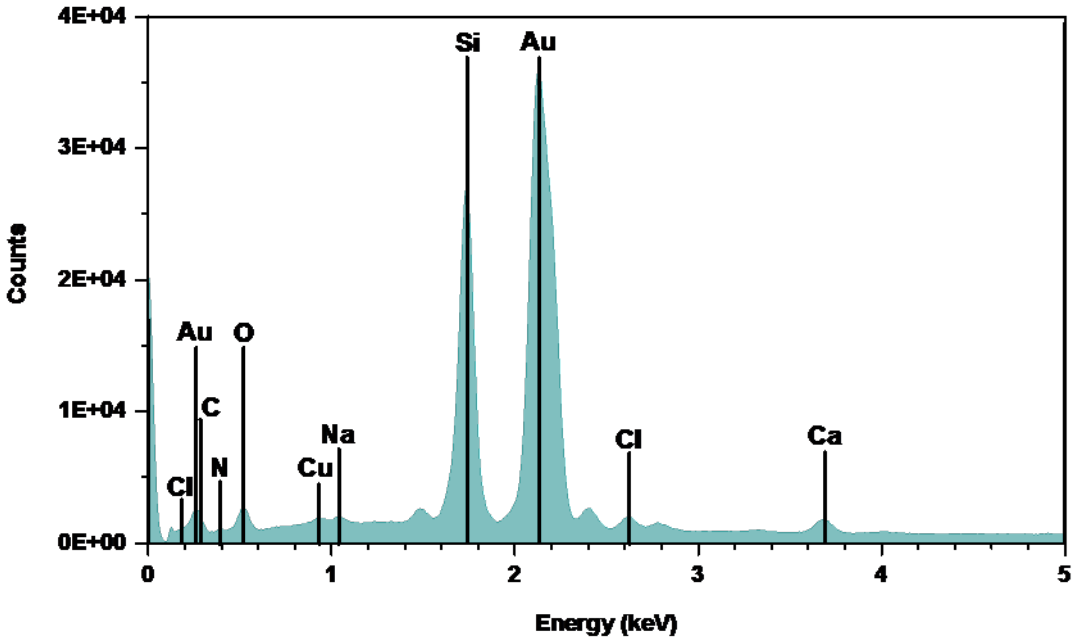

Figure S11. EDS profile shows a strong Au signal along with weak nitrogen (N) and carbon (C) peaks, originating from the αRep molecules bound to the surface of the gold nanoparticles. The silicon (Si) and oxygen (O) signals appear from the SiO2 support grid, and copper (Cu)from the surface contamination. Peaks due to sodium (Na), calcium (Ca), chlorine (Cl) can be attributed to buffer system used for the proteins.

S12. Core-Satellite assembly on streptavidinylated nanostructures

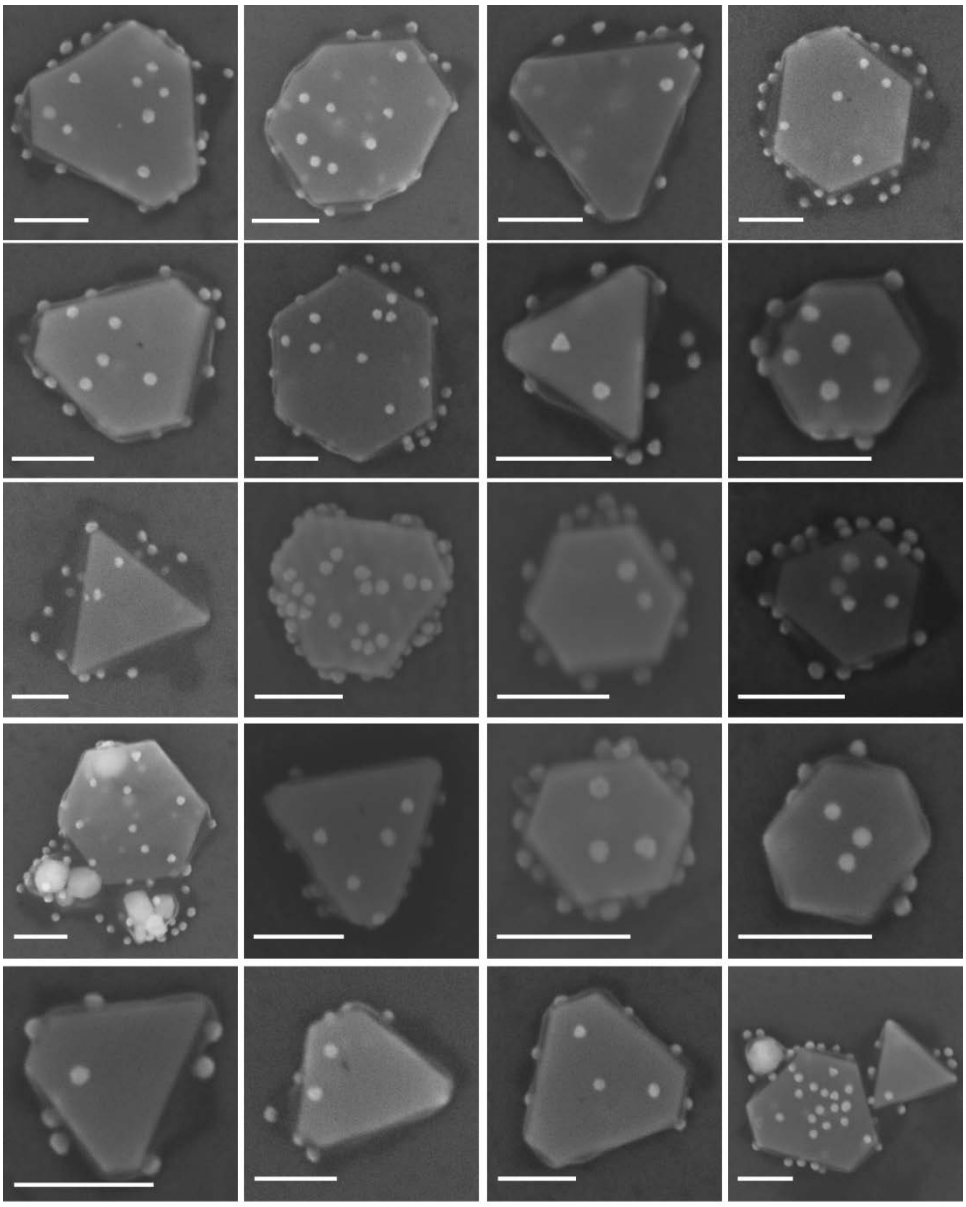

Figure S12. Representative SEM micrographs showing core-satellite assemblies produced by co-incubation of biotinylated Au nanospheres with streptavidinylated G8-capped Au nanocrystals. (Scale bar: 100 nm)

S13. On-surface DAB encapsulation on HRP-functionalized streptavidinylated nanostructures

αRep capped gold nanoparticles can be upgraded to multifunctional catalytic platforms by the attachment of biotinylated enzymes onto the secondary streptavidin layer. Biotinylated-horse radish peroxidase (Biotin-HRP) enzyme is complexed with streptavidin-functionalized Au nanocrystals and surface-confined catalysis of aromatic benzidines is performed. Figure S13a shows multiple examples Au nanocrystals immobilised on an SiO_2/Si substrate prior to induction of the HRP-catalyzed oxidative polymerisation of 1 mM 3,3'-diaminobenzidine (DAB)[23] in presence of H_2O_2 which results in the in-situ precipitation of a polyDAB shell. The water insoluble polymeric DAB layer[24] of uniform thickness (23 ± 3) can be clearly observed around Au nanocrystals (See also panel (a) of Figure S13b).

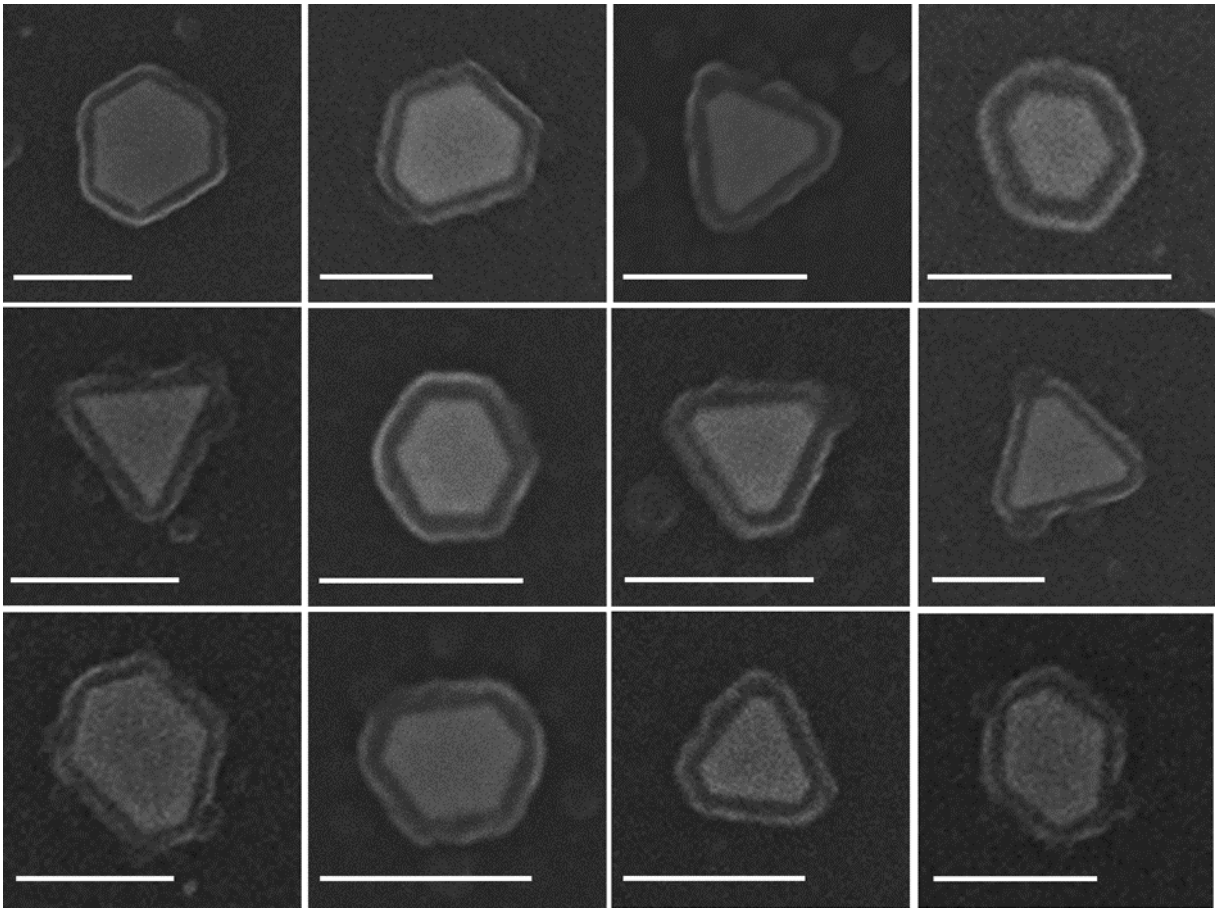

Figure S13a. Representative SEM micrographs showing polymeric DAB shell formed around HRP-Au nanocrystals through catalytic oxidation of 1mM 3,3' diaminobenzidine after a reaction time of 3h. (Scale bars: 200 nm)

The oxidation of DAB molecules on the surface of HRP-Au nanocrystals is also monitored in solution by UV-visible spectroscopy. In Figure S13b(b), the continuous red shifting of the plasmon resonance peak reveals the gradual development of the polymeric DAB shell around the Au nanoparticles. This shift is limited when the DAB precursor concentration is low (1 mM). But for a DAB concentration 20μM DAB, a larger build-up of the polymerized DAB layer leads to a 25 nm

red shift in agreement with the ca. 25 nm thickness of the high index medium observed by SEM on the nanocrystals. Interestingly, as the shell grows and the coated Au nanocrystals become more hydrophobic, they tend to slowly coalesce together into water-insoluble aggregates which can be monitored by the continuous decline in plasmon peak intensity as displayed in Figure S13b(c). The effective HRP catalysis reflects the stability of surface-bound enzymes and could be harnessed for multple on-surface sensing applications.

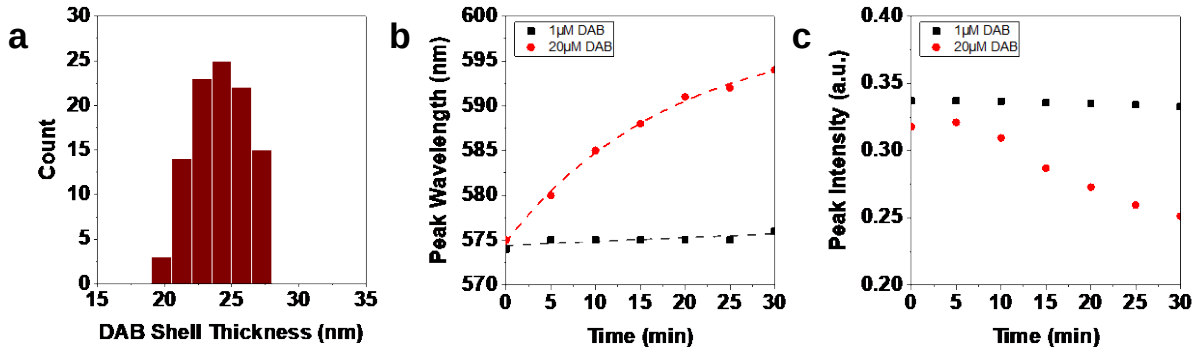

Figure S13b. Characterisation of *on-surface* DAB catalysis by HRP conjugated αRep-Au nanocrystals. (a) Polymeric DAB shell thickness encapsulating Au nanocrystals immobilized on a SiO_2/Si substrate. (b) Spectral shift of the plasmon resonance of Au nanocrystals during solution phase DAB polymerisation reaction for two bulk concentrations of the DAB monomer (1 and 20 μM in black and red respectively). (c) Time evolution of the plasmon resonance peak intensity as the HRP-induced, on-surface DAB polymerization proceeds. The observed intensity decline is due to the coalescence of water-insoluble Au nanocrystals as they become more hydrophobic due to the DAB encapsulation.

S14. References

1 Guellouz, A. *et al.* Selection of Specific Protein Binders for Pre-Defined Targets from an Optimized Library of Artificial Helicoidal Repeat Proteins (alphaRep). *PLoS One* **8**, e71512, (2013).

2 Binz, H. K., Amstutz, P. & Pluckthun, A. Engineering novel binding proteins from nonimmunoglobulin domains. *Nat. Biotechnol.* **23**, 1257-1268, (2005).

3 Boersma, Y. L. & Pluckthun, A. DARPins and other repeat protein scaffolds: advances in engineering and applications. *Curr. Opin. Biotechnol.* **22**, 849-857, (2011).

4 Johnson, C. L. *et al.* Effects of elastic anisotropy on strain distributions in decahedral gold nanoparticles. *Nat. Mater.* **7**, 120-124, (2008).

5 Leger, C. *et al.* Ligand-induced conformational switch in an artificial bidomain protein scaffold. *Scientific Reports* **9**, 1178, (2019).

6 Oshannessy, D. J. & Winzor, D. J. Interpretation of deviations from pseudo-first-order kinetic behavior in the characterization of ligand binding by biosensor technology. *Analytical Biochemistry* **236**, 275-283, (1996).

7 Nedelkov, D. & Nelson, R. W. Practical considerations in BIA/MS: optimizing the biosensor-mass spectrometry interface. *Journal of Molecular Recognition* **13**, 140-+, (2000).

8 Duan, X. *et al.* Quantification of the affinities and kinetics of protein interactions using silicon nanowire biosensors. *Nature Nanotechnology* **7**, 401, (2012).

9 Rostova, E., Ben Adiba, C., Dietler, G. & Sekatskii, S. K. Kinetics of Antibody Binding to Membranes of Living Bacteria Measured by a Photonic Crystal-Based Biosensor. *Biosensors-Basel* **6**, (2016).

10 Oshannessy, D. J., Brighamburke, M., Soneson, K. K., Hensley, P. & Brooks, I. Determination of Rate and Equilibrium Binding Constants for Macromolecular Interactions Using Surface Plasmon Resonance: Use of Nonlinear Least Squares Analysis Methods. *Analytical Biochemistry* **212**, 457-468, (1993).

11 Gorlatova, N. *et al.* Protein Characterization of a Candidate Mechanism SNP for Crohn's Disease: The Macrophage Stimulating Protein R689C Substitution. *PLoS One* **6**, e27269, (2011).

12 Grzelczak, M., Perez-Juste, J., Mulvaney, P. & Liz-Marzan, L. M. Shape control in gold nanoparticle synthesis. *Chemical Society Reviews* **37**, 1783-1791, (2008).

13 Scarabelli, L., Sánchez-Iglesias, A., Pérez-Juste, J. & Liz-Marzán, L. M. A "Tips and Tricks" Practical Guide to the Synthesis of Gold Nanorods. *The Journal of Physical Chemistry Letters* **6**, 4270-4279, (2015).

14 Jana, N. R., Gearheart, L. & Murphy, C. J. Evidence for Seed-Mediated Nucleation in the Chemical Reduction of Gold Salts to Gold Nanoparticles. *Chemistry of Materials* **13**, 2313-2322, (2001).

15 Sirajuddin *et al.* The formation of gold nanoparticles using hydroquinone as a reducing agent through a localized pH change upon addition of NaOH to a solution of HAuCl4. *Colloids and Surfaces A: Physicochemical and Engineering Aspects* **370**, 35-41, (2010).

16 Zhou, J., Zeng, J., Grant, J., Wu, H. & Xia, Y. On-Chip Screening of Experimental Conditions for the Synthesis of Noble-Metal Nanostructures with Different Morphologies. *Small* **7**, 3308-3316, (2011).

17 Wang, Z. *et al.* pH-Dependent Evolution of Five-Star Gold Nanostructures: An Experimental and Computational Study. *ACS Nano* **7**, 2258-2265, (2013).

18 Xie, J., Lee, J. Y. & Wang, D. I. C. Synthesis of Single-Crystalline Gold Nanoplates in Aqueous Solutions through Biomineralization by Serum Albumin Protein. *The Journal of Physical Chemistry C* **111**, 10226-10232, (2007).

19 Liu, B., Xie, J., Lee, J. Y., Ting, Y. P. & Chen, J. P. Optimization of High-Yield Biological Synthesis of Single-Crystalline Gold Nanoplates. *The Journal of Physical Chemistry B* **109**, 15256-15263, (2005).

20 Kumari, M. *et al.* Physico-Chemical Condition Optimization during Biosynthesis lead to development of Improved and Catalytically Efficient Gold Nano Particles. *Scientific Reports* **6**, 27575, (2016).

21 Fang, G., Yang, Y., Yao, J., Shao, Z. & Chen, X. Formation of different gold nanostructures by silk nanofibrils. *Materials Science and Engineering: C* **64**, 376-382, (2016).

22 Bolisetty, S. *et al.* Amyloid-mediated synthesis of giant, fluorescent, gold single crystals and their hybrid sandwiched composites driven by liquid crystalline interactions. *Journal of Colloid and Interface Science* **361**, 90-96, (2011).
23 Chen, S., Svedendahl, M., Van Duyne, R. P. & Käll, M. Plasmon-Enhanced Colorimetric ELISA with Single Molecule Sensitivity. *Nano Letters* **11**, 1826-1830, (2011).
24 Klibanov, A. M., Tu, T.-M. & Scott, K. P. Peroxidase-Catalyzed Removal of Phenols from Coal-Conversion Waste Waters. *Science* **221**, 259, (1983).